APPLIED PHYSICS

Real-time visualization of the laser-plasma wakefield dynamics

Yang Wan[1,2]*, Sheroy Tata[1], Omri Seemann[1], Eitan Y. Levine[1], Eyal Kroupp[1], Victor Malka[1]

The exploration of new acceleration mechanisms for compactly delivering high-energy particle beams has gained great attention in recent years. One alternative that has attracted particular interest is the plasma-based wakefield accelerator, which is capable of sustaining accelerating fields that are more than three orders of magnitude larger than those of conventional radio-frequency accelerators. In this device, acceleration is generated by plasma waves that propagate at nearly light speed, driven by intense lasers or charged particle beams. Here, we report on the direct visualization of the entire plasma wake dynamics by probing it with a femtosecond relativistic electron bunch. This includes the excitation of the laser wakefield, the increase of its amplitude, the electron injection, and the transition to the beam-driven plasma wakefield. These experimental observations provide first-hand valuable insights into the complex physics of laser beam–plasma interaction and demonstrate a powerful tool that can largely advance the development of plasma accelerators for real-time operation.

INTRODUCTION

The use of plasma waves powered by intense laser pulses or relativistic charged particle beams is gaining particular attention as a potential next-generation accelerator for various applications in medicine, material sciences, and high-energy physics (*1*–*3*). In a laser wakefield accelerator (LWFA) (*4*), the plasma electrons are pushed away from the ion background by the ponderomotive force of the drive laser and then pulled back by the space-charge force of the ions, forming behind the driver a trailing plasma wake, which provides both longitudinally accelerating and transversely focusing fields with large magnitudes. Another approach, the plasma wakefield accelerator (PWFA) (*5*), relies on the space-charge force of the relativistic drive bunch of charged particles. Recently, several groups have been able to use an LWFA accelerated electron bunch to drive its own PWFA (*6*, *7*), creating an ultra-compact module known as the hybrid laser-plasma wakefield accelerator (*8*). All these approaches have made great breakthroughs in the past decades, including the first 100 s of MeV to multi-GeV acceleration of electrons and positrons with narrow energy spreads (*9*–*13*), high wake-to-beam energy transfer efficiency (*14*, *15*), and the demonstration of free electron lasing based on plasma accelerators (*16*–*18*). Despite these tremendous progress, there is still a critical challenge in optimizing the accelerator performance to enhance the beam quality and stability due to the complex and nonlinear interplay between intense lasers, relativistic electron bunches, and background plasma (*3*, *19*). Consequently, it is becoming increasingly essential to directly monitor the dynamics of the wakefield at each stage of propagation in real time, which is crucial for understanding the subtle yet key physical processes such as wave excitation, electron injection, and the transition between accelerator staging (*20*).

Earlier diagnostic techniques primarily rely on optical laser pulses, such as frequency domain interferometry (*21*) and optical shadowgraphy (*6*, *22*, *23*), which have been widely used to measure the period of the plasma wave (*21*–*24*), the length of the electron bunch (*22*), and the strength of the magnetic field (*22*, *25*). A newly developed technique called femtosecond relativistic electron microscopy (FREM) offers an alternative approach for diagnostics (*26*, *27*). By using electron beams generated from laser-plasma as a probe, FREM enables measurements of highly transient, microscopic field structures like plasma wakefields with high spatiotemporal resolution, owing to its few femtosecond pulse durations (*22*, *28*, *29*), micrometer-scale source sizes (*30*, *31*), and relativistic particle energies. Additionally, the electron probe encompasses several distinctive properties. First, it is capable of detecting both electric and magnetic fields, providing complementary insights into the shadowgraphic technique, which is sensitive to plasma density due to refraction and magnetic fields due to Faraday effect. Second, the electron probe can measure the plasma wake structure across a wide range of plasma densities (from 10^{16} to 10^{19} cm^{-3}), whereas optical pulses are mostly used in higher density regions. Last, the electron probe is highly sensitive to the space-charge fields of the charged particle bunch. Leveraging these unique properties, FREM has been successfully used to probe the linear structure of wakefields (*26*), the rear spikes of nonlinear wakefields (*27*), and electron bunches in plasma (*31*), and an algorithm for field reconstruction was also recently developed (*32*). Yet, a comprehensive experimental investigation of the entire evolution of the plasma wakefield from its excitation until the end remains elusive, of which the explanation still mostly relies on the support from computationally expensive postprocessing numerical simulations.

Here, we report on the direct characterization of the complete dynamics of the plasma waves throughout its propagation along the gas jet, which is first driven by a laser pulse and then by the laser-accelerated electron bunch, using the technique FREM (see Fig. 1). Previously, such a transition can only be deduced indirectly from the electron energy spectra (*33*–*35*) and betatron x-ray emission (*36*).

RESULTS

The experiment was conducted using the HIGGINS dual 100-TW laser system at the Weizmann Institute of Science (*37*). In the experimental setup, one laser beam with 1.2-J and 30-fs duration was focused onto a 3-mm-long helium gas jet doped with 1% nitrogen, resulting in the stable production of an ultra-relativistic electron bunch as a probe. Averaged over 30 shots, the probe bunch was found to have a

[1]Department of Physics of Complex Systems, Weizmann Institute of Science, Rehovot 7610001, Israel. [2]School of Physics, Zhengzhou University, Zhengzhou 450001, China.
*Corresponding author. Email: yang.wan@weizmann.ac.il, yangwan23@zzu.edu.cn

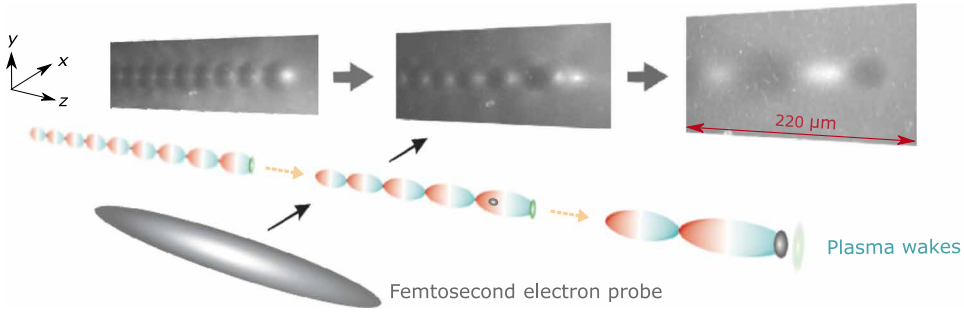

Fig. 1. Schematic experimental setup. An intense laser pulse (green ellipsoid) was focused on a gaseous target and drove a plasma wakefield behind it. After propagating a few millimeter distance, electrons (small gray sphere) were injected into the first wake bucket and got accelerated. Near the rear downramp of the gas target, the laser intensity became too weak to drive a strong wakefield and the electron bunch–driven wakefield started to be dominant. The abovementioned dynamics were captured by using another electron beam generated from the same type of laser-plasma accelerator. The probe beam (large gray ellipsoid) was deflected by the plasma and electron bunch's fields and then impinged on a 50-μm-thick Ce:YAG screen after an 8-mm drift. The recorded probe density modulations (raw data, gray colormap) on the imaging screen of three different positions resemble the investigated wakefield and electron bunch's structures.

quasi-monoenergetic energy spectrum with a peak at 295 ± 30 MeV and an FWHM (full width at half maximum) spread of 60 ± 25 MeV (see fig. S1 for the probe bunch experimental data). Although not measured directly in the experiment, the probe bunch duration was estimated from simulations to be around 2 fs in root mean square (RMS). After exiting the gas jet, the probe bunch then drifted in vacuum for 10 cm and laterally expanded into several hundreds of micrometers in size, intercepting perpendicularly the laser- or beam-driven wakefield to be probed and getting deflected. After an additional drift of 8 mm, these deflections manifested as periodic patterns in the probe bunch density, directly reflecting the plasma field information. A thin Ce:YAG scintillator and a high-resolution optical system were used to image the density-modulated probe bunch.

The wakefield under investigation was produced by focusing a second 1-J, 30-fs laser beam onto a 3-mm-long gas jet with the same helium/nitrogen mixture. The peak plasma density was around 2.5×10^{18} cm^{-3}, well below the self-injection threshold (*38*, *39*), and the electrons were injected through ionization (*40*, *41*) and then accelerated up to 100 MeV with a continuous spectrum. The charge above 30 MeV, estimated from the calibrated spectrometer, was 24 ± 7 pC, averaged over 30 shots. As will be discussed below, the electron probe used in the experiment was capable of distinguishing between the laser and particle contributions to the wakefield without ambiguity, eliminating the need for an external thin foil to block the residual laser. It is worth noting that the two high-power laser pulses were generated from the same system, ensuring perfect synchronization between the electron probe bunch and the probed wakefield, with a temporal jitter of around 10 fs (*27*). More details about the experimental setup can be found in Materials and Methods.

By slightly varying the probe propagation direction and correspondingly adjusting the delay with the pump laser, we captured the driven plasma wave evolution at different positions. Figure 2A shows the longitudinal plasma density profile extracted from the computational fluid dynamic simulation using the same nozzle design as the experiment, where $z = 0$ is defined as the jet center and the laser propagates in the positive direction. Snapshots of the wakefield images are presented in Fig. 2B, where $\delta n/n_0$ represents the relative density modulation of the probe with n_0 the background obtained by smoothing the raw data through a low-order Gaussian filter and δn the absolute density variation caused by the wakefield. We note that for the presented shots, the electron bunches generated from the investigated wakefields were ensured to have similar energy distributions and charges for self-consistency (see fig. S2 for the characterization of the accelerated electron beams).

According to the experimental snapshots, the wakefield evolution can be divided into three stages. The first stage is the laser wakefield stage before injection (Fig. 2, B1 to B5). As shown in Fig. 2 (B1 and B2), when a short intense laser pulse reaches the up ramp of the gas target, it ionizes the surrounding gas and launches a trailing plasma wave, which is consistent with the observation that the wakefield period decreases from the tail to the head. Moreover, the probe images show similar length and intensity amplitude between the bright and dark regions of the plasma wake, indicating that the launched plasma wave is quasi-linear (*21*, *26*). The transverse wave shape is flat for the first several wave buckets and becomes more curved at later periods, which is due to the electron transverse phase mixing in plasma (*42*). As the drive laser reaches the plateau region (Fig. 2B3), the transverse scale of the plasma wave reduces, whereas both the strength and curvature of the wave increase, suggesting that the drive laser is undergoing strong self-focusing (*43*–*45*), resulting in a nonlinear plasma wake. Thereafter, the self-focusing process continues and the wakefield strength keeps increasing (Fig. 2, B4 and B5).

The second stage involves electron injection in LWFA and its impact on the laser wakefield (Fig. 2, B6 and B7). Once the wakefield strength is large enough, electrons ionized from the inner shell of the nitrogen atom start to get trapped and accelerated in the wave bucket (*40*, *41*). With regard to the probe beam that traverses the wakefield, the ion cavity or the so-called "plasma bubble" provides a focusing effect, while the injected electron bunch locally repels the probe particles, leading to a tiny shaded area surrounded by a bright region in the first period of the wakefield image of Fig. 2B6. Moreover, the wakefield period enlarges from the tail to the head, indicating that the injection occurs near the rear gas target downramp. As the laser pulse propagates further along the rear down ramp of the plasma target, its intensity reduces due to diffraction, whereas the ionization injection continues, and the electron beam charge keeps increasing (see fig. S3 for the simulated laser and electron bunch evolution), which means that the laser wakefield becomes weaker and the bunch space-charge fields become stronger. Consequently, the small shaded area of the first wave bucket shown in the probe image turns into a much more pronounced dark hollow (see Fig. 2B7).

Later on, the intensity of the laser pulse decreases steadily along the downramp, leading to a shift of the plasma wave's dominant driver

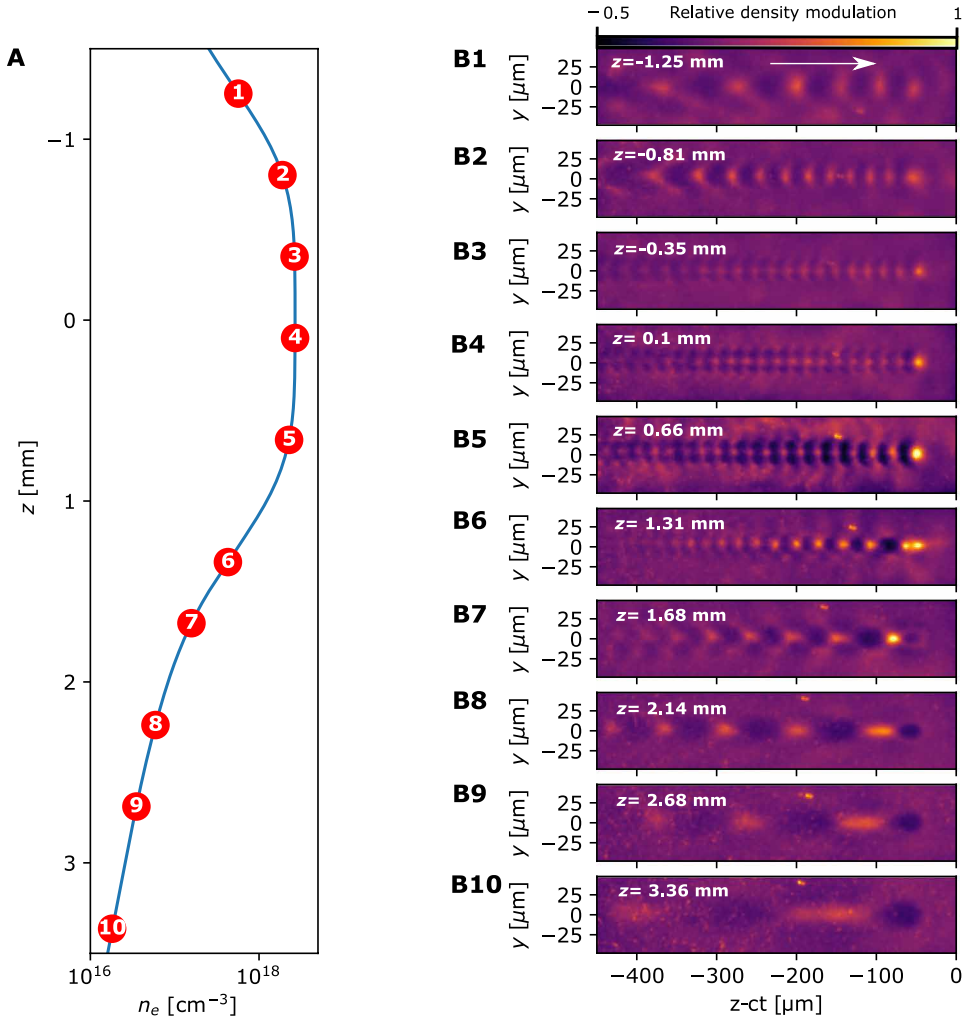

Fig. 2. Experimental visualization of the wakefield dynamics at 10 different positions. (**A**) Probed positions along the gas target and its corresponding plasma density (log scale). (**B1** to **B10**) Experimental snapshots of the plasma wake at the positions in the plasma marked in (A). The white arrow in the first subplot indicates the wake propagation direction.

toward the electron bunch (Fig. 2B8). This was confirmed by slightly reducing the input laser energy to avoid ionization injection, which revealed that the strength of the wakefield was notably weaker compared to that observed with an injected electron beam. Furthermore, the elliptical hollow structure preceding the wakefield was recently discovered to resemble the transverse charge-density distribution of the electron bunch (*31*). On the basis of this understanding, it is shown that, as the bunch propagates further into the density downramp (Fig. 2, B9 and B10), its transverse sizes gradually increase due to the weakening of the plasma focusing force (*31*, *46*). Additionally, the transverse scale of the wakefield (represented by the trailing periodic bright-dark pattern) also increases along with the drive electron beam, behaving as a quasi-linear beam-driven plasma wave (*47*).

To validate the above experimental observations, we have performed high-resolution quasi–three-dimensional particle-in-cell (3D PIC) simulations using the code FBPIC (*48*) with the same laser and plasma parameters as those used in the experiment for modeling the entire process (see Materials and Methods for more details of the simulation setup). Figure 3A presents the distributions of the simulated electron density and the laser electric field at the same 10 positions appearing in Fig. 2. Impressively, one can observe similar wakefield dynamics as in the experiment. At each position, we further add a high-energy electron probe bunch into the simulation. After traversing the wakefield and another drift of 8 mm, the density modulation of the probe bunch is plotted in Fig. 3B. Comparing each of them with the cropped experimental snapshot presented in Fig. 3C shows quite good agreement. The small difference, mainly occurring in the subfigures between the fourth to the sixth, could come from the fact that our simulations applied the laser pulse with ideal spatial and spectral profiles, which typically enhance the laser self-focusing effect and also the injection performance.

Let us now use the linear pertubation model given by (*31*, *32*) to estimate the evolution of the wakefield strength from the experimental data presented in Fig. 2B. This model assumes the cylindrical symmetry of the wakefield and neglects the magnetic field contributions for simplicity (see Materials and Methods). Figure 4 shows the estimated amplitudes of the longitudinal electric field E_z of the first wake period (red solid squares) at several positions along the gas jet

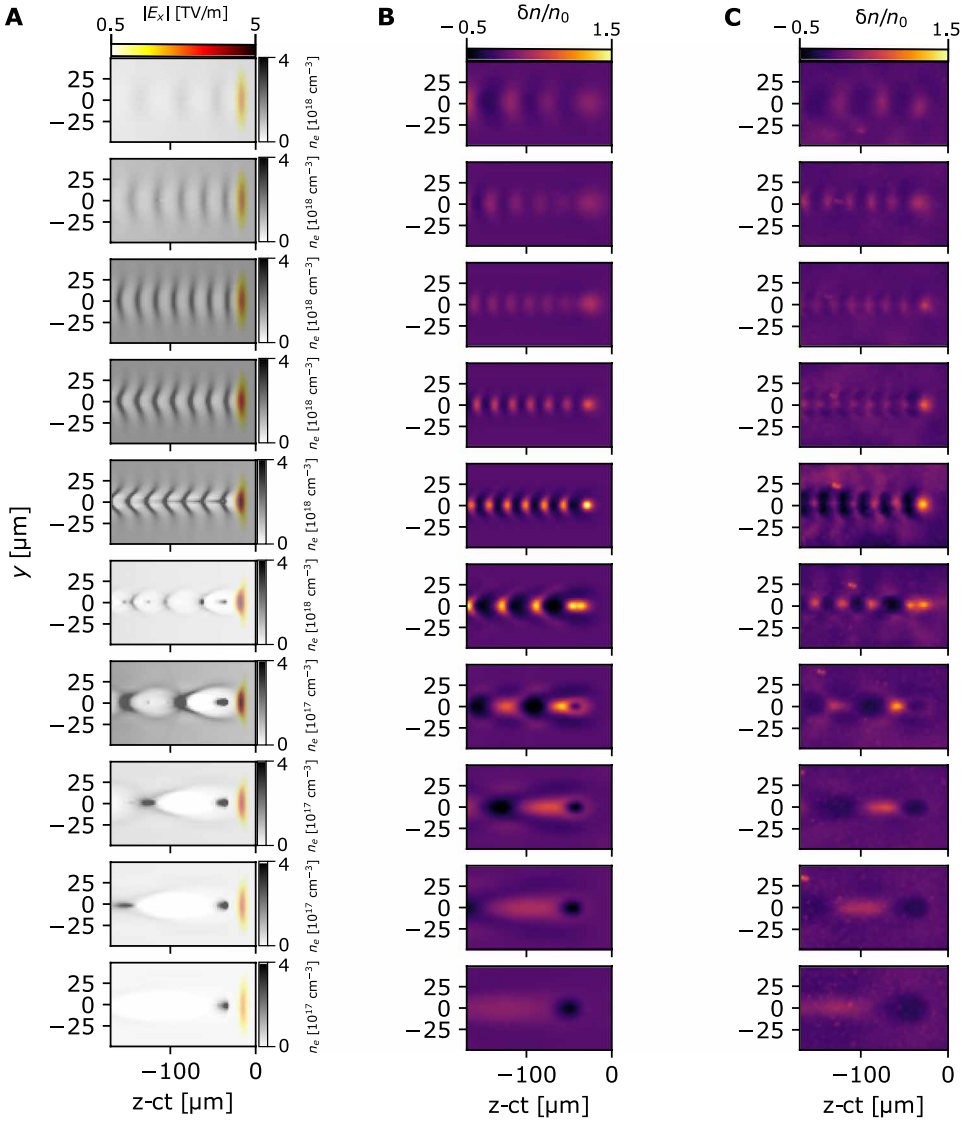

Fig. 3. PIC simulations of the wakefield dynamics and the comparison with experimental observations. (**A**) Distributions of the simulated electron density (gray colormap) and the laser electric field (yellow-red colormap) at the 10 positions corresponding to Fig. 2A. (**B**) Simulated probe relative density modulations of (A). (**C**) Experimental probe relative density modulations for comparison.

front upramp (Fig. 2, B1 and B2) and rear downramp (Fig. 2, B7 to B10). For comparison, the evolution of the simulated E_z from the same wave period is plotted as the green solid line, showing a relatively good agreement with the experimental value. It is noted that for the probe images of Fig. 2 (B3 to B6), the strength of the wakefield captured at these positions becomes so intense that a large fraction of probe electrons after an 8-mm drift already cross each other's trajectories. In this case, the system becomes nonlinear and we cannot use the linear algorithm (such as the above one) to retrieve the field structures.

DISCUSSION

Here, we have presented the first experimental filming of the laser wakefield evolution and its final transition to a beam-driven wakefield, which has allowed us to uncover a complete story of a laser-plasma

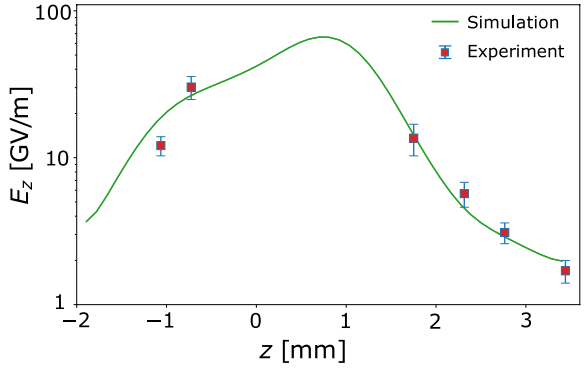

Fig. 4. Estimated wakefield strength along the propagation throughout the gas jet and comparison with PIC simulation.

accelerator, starting from the moment the laser enters the gas target and ending with a relativistic electron bunch exiting the plasma. By using a laser-plasma–accelerated high-energy electron bunch as a high-resolution probe, the FREM enables us to get valuable insights into many important processes including laser relativistic self-focusing, plasma wave amplitude growth, electron injection in laser wakefield, and the dominance of beam-driven wakefield. All in a single experimental setup. Furthermore, the recorded experimental observations of wakefield propagation, spanning nearly 5 mm, show good agreements with a large-scale 3D PIC simulation. This signifies that researchers can now directly obtain crucial but subtle information about each position from experiments, thereby greatly reducing their reliance on computationally expensive numerical simulations. The results of this study offer substantial potential for guiding the real-time fine-tuning of different types of plasma accelerators including LWFA, PWFA, and staged LWFA-PWFA. The versatility of this technique allows for its integration into various high-power laser laboratories and large facilities such as ELI, EuPRAXIA, CERN, SLAC, and DESY, strengthening our belief that it will revolutionize the fields of experimental plasma and accelerator physics.

MATERIALS AND METHODS

Laser system

The experiment was carried out at the HIGGINS dual 100-TW laser platform at the Weizmann Institute of Science (*37*), where a 1-Hz, 7-J laser beam was split into two equal parts after the final amplifier: laser A for the acceleration of the probe electron bunch, and laser B for driving the wakefield. Both lasers were independently compressed to 30-fs durations and focused to 28.5- and 37.8-μm spots (FWHM), respectively. In the experiment, the used laser energies on target were ~1.2 J and ~1 J, respectively.

Generation and characterization of the two LWFA electron beams

The electron probe beam was generated by focusing laser A onto a supersonic flow from a 3-mm-diameter nozzle, where the gas was a mixture of around 99% helium and 1% nitrogen. Peak plasma density along the laser path was 1×10^{19} cm^{-3} as measured by an off-line Mach-Zehnder interferometer and assuming complete ionization. The probe bunch contained a quasi-monoenergetic spectrum with a peak energy of 295 ± 30 MeV and an FWHM energy spread of 60 ± 25 MeV. Its angular RMS divergences were 3.2 ± 1.3 mrad in the horizontal direction and 2.5 ± 0.8 mrad in the vertical direction, and the total charge above 200 MeV was 267 ± 58 pC. The detailed data of the probe spectra and angular profiles are presented in fig. S1.

The probed wakefield was launched by laser B by focusing it onto a supersonic flow from a 3-mm-diameter nozzle of the same gas mixture. The gas density profile used in this work was extracted from a computational fluid dynamics (CFD) simulation (ANSYS FLUENT) with the same nozzle design. The peak plasma density for the study of wakefield evolution was around 2.5×10^{18} cm^{-3} after full ionization. The ionization injected electron bunch was accelerated up to 100 MeV with a continuous spectrum. The charge above 30 MeV estimated from the calibrated spectrometer was 24 ± 7 pC. Images of experimental data for the electron energy spectra are presented in fig. S2.

The data statistics of the two electron beams' charge and energy spectra were measured using 30 consecutive shots before performing the actual pump-probe experiment, and the error bars come from shot-to-shot fluctuation, Lanex calibration uncertainty (*49*), and measurement errors such as divergence-induced position uncertainty in the energy spectrometer.

High-resolution imaging system

The probe beam profile, with variations created by the plasma fields, was recorded onto a 50-μm-thick Ce:YAG scintillating screen placed 8 mm away from the second jet with a 100-μm-thick stainless steel foil in front of it for blocking the residual laser. The image on the screen was then transmitted by a combination of a long working-distance plan-apochromatic microscope objective and an achromatic lens with $f = 200$ mm to a 16-bit scientific Complementary Metal Oxide Semiconductor (sCMOS) camera. The resolution, defined as the RMS size of the point-spread function, was estimated to be around 1 μm, which is dertermined by four factors: the thickness of the YAG crystal, the resolution of the optical system, the thickness of the blocking foil, and the size of the probe source. Among them, the YAG crystal thickness is the primary limiting factor. This is because when the probe travels through the crystal, light emissions from the entire path mix with each other. By reducing the crystal thickness to half, the resolution can be enhanced to around 0.5 μm, but the signal intensity will decrease as well. Furthermore, increasing the probe electron energy or placing the YAG crystal closer to the probed wakefield can also be beneficial, which allows the probe electrons to avoid nonlinear trajectory crossings and enables the quantitative reconstruction of the field structures.

PIC simulations

PIC simulations were done using the pseudo-spectral code FBPIC (*48*) with a quasi-cylindrical geometry simulated with $N_m = 5$ azimuthal modes. In the simulation presented in Fig. 3C and fig. S3, the cylindrical simulation box had 300-μm length and 80-μm radius with a mesh of $\Delta z = 40$ nm and $\Delta r = 320$ nm. The laser driver (pulse B) was initialized with Gaussian temporal and spatial profiles of 30-fs (FWHM) duration and 38-μm (FWHM) spot size and focused at the entrance of the gas plateau region with a normalized amplitude of $a_0 = 1.05$, corresponding to a laser of 1.17 J on target. The gas profile was extracted from the CFD simulation with the same mixture with a peak plasma density of $n_e = 2.5 \times 10^{18}$ cm^{-3} after full ionization. In this simulation, the first electron from the helium atom and five electrons from the L shell of the nitrogen atom were set pre-ionized. The modeling window first co-propagated with the drive laser, and we recorded the simulation states (i.e., checkpoints) at multiple positions along the propagation. These checkpoints allowed us to restart the simulation at these positions self-consistently with a stationary modeling window and with added probe particles from one transverse boundary. The probe bunch had a $\tau_{probe} = 2$-fs duration (estimated from another PIC simulation solely for the probe generation in an LWFA), with a peak energy of 300 MeV and 20% FWHM energy spread. The probe divergence was set the same as in the experiment, and the number of macroparticles in the bunch was chosen to be 2×10^7.

Reconstruction of the longitudinal electric wakefields

For the probe images taken at positions along the gas jet front upramp (Fig. 2, B1 and B2) and rear downramp (Fig. 2, B7 to B10), the investigated wakefield is mostly under the quasi-linear or weakly nonlinear regime, and also the trajectory crossing between the probe electrons does not occur yet. Therefore, we can ignore the magnetic field components and reconstruct the electric wakefields based on the linear model given by (*32*). This model assumes that the wakefield

propagating along the z direction is in cylindrical symmetry (r, z). After crossing the wakefield along the x direction and further drifting a distance of L, the relative density modulation $\delta n/n_0$ of the probe, if the value is small enough, can be expressed as

$$I(y,z) = \frac{\delta n}{n_0}(y,z) \simeq \kappa \nabla \cdot \int_{-\infty}^{+\infty} \mathbf{E}(z-x,r)dx \quad (1)$$

where $\kappa = eL/Mcp_0$ is the coefficient with e the electron charge, c the light speed in vacuum, ϵ_0 the vacuum permittivity, and M the geometric magnification ($M = 1.08$ in our experiment). For a driver with transverse Gaussian profile, by taking the derivative of Eq. 1 along z and applying the Panofsky-Wenzel theorem, one can obtain a simple relation as follows

$$\frac{\partial I(y,z)}{\partial z} \simeq \kappa \mathbf{e}^{-(k_p\Delta_x)^2/2}\nabla^2 \int_{-\infty}^{+\infty} E_z(z,r)dx \quad (2)$$

where k_p is the plasma wave number and Δ_x is the RMS transverse size of the plasma wave, both of which can be obtained directly from the probe image. By solving the Poisson equation of Eq. 2 and then performing Abel inversion, the longitudinal electric wakefield E_z can be calculated.

Supplementary Materials

This PDF file includes:
Figs. S1 and S3
Legend for movie S1

Other Supplementary Material for this manuscript includes the following:
Movie S1

REFERENCES AND NOTES

1. V. Malka, J. Faure, Y. A. Gauduel, E. Lefebvre, A. Rousse, K. T. Phuoc, Principles and applications of compact laser–plasma accelerators. *Nat. Phys.* **4**, 447–453 (2008).
2. S. M. Hooker, Developments in laser-driven plasma accelerators. *Nat. Photonics* **7**, 775–782 (2013).
3. C. Joshi, S. Corde, W. B. Mori, Perspectives on the generation of electron beams from plasma-based accelerators and their near and long term applications. *Phys. Plasmas* **27**, 070602 (2020).
4. T. Tajima, J. M. Dawson, Laser electron accelerator. *Phys. Rev. Lett.* **43**, 267–270 (1979).
5. P. Chen, J. M. Dawson, R. W. Huff, T. Katsouleas, Acceleration of electrons by the interaction of a bunched electron beam with a plasma. *Phys. Rev. Lett.* **54**, 693–696 (1985).
6. M. F. Gilljohann, H. Ding, A. Döpp, J. Götzfried, S. Schindler, G. Schilling, S. Corde, A. Debus, T. Heinemann, B. Hidding, S. M. Hooker, A. Irman, O. Kononenko, T. Kurz, A. Martinez de la Ossa, U. Schramm, S. Karsch, Direct observation of plasma waves and dynamics induced by laser-accelerated electron beams. *Phys. Rev. X* **9**, 011046 (2019).
7. T. Kurz, T. Heinemann, M. F. Gilljohann, Y. Y. Chang, J. P. Couperus Cabadağ, A. Debus, O. Kononenko, R. Pausch, S. Schöbel, R. W. Assmann, M. Bussmann, H. Ding, J. Götzfried, A. Köhler, G. Raj, S. Schindler, K. Steiniger, O. Zarini, S. Corde, A. Döpp, B. Hidding, S. Karsch, U. Schramm, A. Martinez de la Ossa, A. Irman, Demonstration of a compact plasma accelerator powered by laser-accelerated electron beams. *Nat. Commun.* **12**, 2895 (2021).
8. B. Hidding, T. Königstein, J. Osterholz, S. Karsch, O. Willi, G. Pretzler, Monoenergetic energy doubling in a hybrid laser-plasma wakefield accelerator. *Phys. Rev. Lett.* **104**, 195002 (2010).
9. J. Faure, Y. Glinec, A. Pukhov, S. Kiselev, S. Gordienko, E. Lefebvre, J.-P. Rousseau, F. Burgy, V. Malka, A laser–plasma accelerator producing monoenergetic electron beams. *Nature* **431**, 541–544 (2004).
10. S. P. D. Mangles, C. D. Murphy, Z. Najmudin, A. G. R. Thomas, J. L. Collier, A. E. Dangor, E. J. Divall, P. S. Foster, J. G. Gallacher, C. J. Hooker, D. A. Jaroszynski, A. J. Langley, W. B. Mori, P. A. Norreys, F. S. Tsung, R. Viskup, B. R. Walton, K. Krushelnick, Monoenergetic beams of relativistic electrons from intense laser–plasma interactions. *Nature* **431**, 535–538 (2004).
11. C. G. R. Geddes, C. Toth, J. Van Tilborg, E. Esarey, C. B. Schroeder, D. Bruhwiler, C. Nieter, J. Cary, W. P. Leemans, High-quality electron beams from a laser wakefield accelerator using plasma-channel guiding. *Nature* **431**, 538–541 (2004).
12. A. J. Gonsalves, K. Nakamura, J. Daniels, C. Benedetti, C. Pieronek, T. C. H. de Raadt, S. Steinke, J. H. Bin, S. S. Bulanov, J. van Tilborg, C. G. R. Geddes, C. B. Schroeder, C. Tóth, E. Esarey, K. Swanson, L. Fan-Chiang, G. Bagdasarov, N. Bobrova, V. Gasilov, G. Korn, P. Sasorov, W. P. Leemans, Petawatt laser guiding and electron beam acceleration to 8 gev in a laser-heated capillary discharge waveguide. *Phys. Rev. Lett.* **122**, 084801 (2019).
13. S. Corde, E. Adli, J. M. Allen, W. An, C. I. Clarke, C. E. Clayton, J. P. Delahaye, J. Frederico, S. Gessner, S. Z. Green, M. J. Hogan, C. Joshi, N. Lipkowitz, M. Litos, W. Lu, K. A. Marsh, W. B. Mori, M. Schmeltz, N. Vafaei-Najafabadi, D. Walz, V. Yakimenko, G. Yocky, Multi-gigaelectronvolt acceleration of positrons in a self-loaded plasma wakefield. *Nature* **524**, 442–445 (2015).
14. M. Litos, E. Adli, W. An, C. I. Clarke, C. E. Clayton, S. Corde, J. P. Delahaye, R. J. England, A. S. Fisher, J. Frederico, S. Gessner, S. Z. Green, M. J. Hogan, C. Joshi, W. Lu, K. A. Marsh, W. B. Mori, P. Muggli, N. Vafaei-Najafabadi, D. Walz, G. White, Z. Wu, V. Yakimenko, G. Yocky, High-efficiency acceleration of an electron beam in a plasma wakefield accelerator. *Nature* **515**, 92–95 (2014).
15. F. M. Foerster, A. Döpp, F. Haberstroh, K. V. Grafenstein, D. Campbell, Y.-Y. Chang, S. Corde, J. P. C. Cabadağ, A. Debus, M. F. Gilljohann, A. F. Habib, T. Heinemann, B. Hidding, A. Irman, F. Irshad, A. Knetsch, O. Kononenko, A. M. de la Ossa, A. Nutter, R. Pausch, G. Schilling, A. Schletter, S. Schöbel, U. Schramm, E. Travac, P. Ufer, S. Karsch, Stable and high-quality electron beams from staged laser and plasma wakefield accelerators. *Phys. Rev. X* **12**, 041016 (2022).
16. W. Wang, K. Feng, L. Ke, C. Yu, Y. Xu, R. Qi, Y. Chen, Z. Qin, Z. Zhang, M. Fang, J. Liu, K. Jiang, H. Wang, C. Wang, X. Yang, F. Wu, Y. Leng, J. Liu, R. Li, Z. Xu, Free-electron lasing at 27 nanometres based on a laser wakefield accelerator. *Nature* **595**, 516–520 (2021).
17. R. Pompili, D. Alesini, M. P. Anania, S. Arjmand, M. Behtouei, M. Bellaveglia, A. Biagioni, B. Buonomo, F. Cardelli, M. Carpanese, E. Chiadroni, A. Cianchi, G. Costa, A. Del Dotto, M. Del Giorno, F. Dipace, A. Doria, F. Filippi, M. Galletti, L. Giannessi, A. Giribono, P. Iovine, V. Lollo, A. Mostacci, F. Nguyen, M. Opromolla, E. Di Palma, L. Pellegrino, A. Petralia, V. Petrillo, L. Piersanti, G. Di Pirro, S. Romeo, A. R. Rossi, J. Scifo, A. Selce, V. Shpakov, A. Stella, C. Vaccarezza, F. Villa, A. Zigler, M. Ferrario, Free-electron lasing with compact beam-driven plasma wakefield accelerator. *Nature* **605**, 659–662 (2022).
18. M. Labat, J. C. Cabadağ, A. Ghaith, A. Irman, A. Berlioux, P. Berteaud, F. Blache, S. Bock, F. Bouvet, F. Briquez, Y.-Y. Chang, S. Corde, A. Debus, C. De Oliveira, J.-P. Duval, Y. Dietrich, M. E. Ajjouri, C. Eisenmann, J. Gautier, R. Gebhardt, S. Grams, U. Helbig, C. Herbeaux, N. Hubert, C. Kitegi, O. Kononenko, M. Kuntzsch, M. L. Berge, S. Lê, B. Leluan, A. Loulergue, V. Malka, F. Marteau, M. H. N. Guyen, D. Oumbarek-Espinos, R. Pausch, D. Pereira, T. Püschel, J.-P. Ricaud, P. Rommeluere, E. Roussel, P. Rousseau, S. Schöbel, M. Sebdaoui, K. Steiniger, K. Tavakoli, C. Thaury, P. Ufer, M. Valléau, M. Vandenberghe, J. Vétéran, U. Schramm, M.-E. Couprie, Seeded free-electron laser driven by a compact laser plasma accelerator. *Nat. Photonics* **17**, 150–156 (2022).
19. E. Esarey, C. B. Schroeder, W. P. Leemans, Physics of laser-driven plasma-based electron accelerators. *Rev. Mod. Phys.* **81**, 1229–1285 (2009).
20. M. C. Downer, R. Zgadzaj, A. Debus, U. Schramm, M. C. Kaluza, Diagnostics for plasma-based electron accelerators. *Rev. Mod. Phys.* **90**, 035002 (2018).
21. N. H. Matlis, S. Reed, S. S. Bulanov, V. Chvykov, G. Kalintchenko, T. Matsuoka, P. Rousseau, V. Yanovsky, A. Maksimchuk, S. Kalmykov, G. Shvets, M. C. Downer, Snapshots of laser wakefields. *Nat. Phys.* **2**, 749–753 (2006).
22. A. Buck, M. Nicolai, K. Schmid, C. M. S. Sears, A. Sävert, J. M. Mikhailova, F. Krausz, M. C. Kaluza, L. Veisz, Real-time observation of laser-driven electron acceleration. *Nat. Phys.* **7**, 543–548 (2011).
23. A. Sävert, S. P. D. Mangles, M. Schnell, E. Siminos, J. M. Cole, M. Leier, M. Reuter, M. B. Schwab, M. Möller, K. Poder, O. Jäckel, G. G. Paulus, C. Spielmann, S. Skupin, Z. Najmudin, M. C. Kaluza, Direct observation of the injection dynamics of a laser wakefield accelerator using few-femtosecond shadowgraphy. *Phys. Rev. Lett.* **115**, 055002 (2015).
24. H. Ding, A. Döpp, M. Gilljohann, J. Götzfried, S. Schindler, L. Wildgruber, G. Cheung, S. M. Hooker, S. Karsch, Nonlinear plasma wavelength scalings in a laser wakefield accelerator. *Phys. Rev. E* **101**, 023209 (2020).
25. M. C. Kaluza, H.-P. Schlenvoigt, S. P. D. Mangles, A. G. R. Thomas, A. E. Dangor, H. Schwoerer, W. B. Mori, Z. Najmudin, K. M. Krushelnick, Measurement of magnetic-field structures in a laser-wakefield accelerator. *Phys. Rev. Lett.* **105**, 115002 (2010).
26. C. J. Zhang, J. F. Hua, Y. Wan, C.-H. Pai, B. Guo, J. Zhang, Y. Ma, F. Li, Y. P. Wu, H.-H. Chu, Y. Q. Gu, X. L. Xu, W. B. Mori, C. Joshi, J. Wang, W. Lu, Femtosecond probing of plasma wakefields and observation of the plasma wake reversal using a relativistic electron bunch. *Phys. Rev. Lett.* **119**, 064801 (2017).
27. Y. Wan, O. Seemann, S. Tata, I. A. Andriyash, S. Smartsev, E. Kroupp, V. Malka, Direct observation of relativistic broken plasma waves. *Nat. Phys.* **18**, 1186–1190 (2022).

28. O. Lundh, J. Lim, C. Rechatin, L. Ammoura, A. Ben-Ismaïl, X. Davoine, G. Gallot, J.-P. Goddet, E. Lefebvre, V. Malka, J. Faure, Few femtosecond, few kiloampere electron bunch produced by a laser–plasma accelerator. *Nat. Phys.* **7**, 219–222 (2011).
29. C. J. Zhang, J. F. Hua, Y. Wan, B. Guo, C.-H. Pai, Y. P. Wu, F. Li, H.-H. Chu, Y. Q. Gu, W. B. Mori, C. Joshi, J. Wang, W. Lu, Temporal characterization of ultrashort linearly chirped electron bunches generated from a laser wakefield accelerator. *Phys. Rev. Accel. Beams* **19**, 062802 (2016).
30. M. Schnell, A. Sävert, B. Landgraf, M. Reuter, M. Nicolai, O. Jäckel, C. Peth, T. Thiele, O. Jansen, A. Pukhov, O. Willi, M. C. Kaluza, C. Spielmann, Deducing the electron-beam diameter in a laser-plasma accelerator using x-ray betatron radiation. *Phys. Rev. Lett.* **108**, 075001 (2012).
31. Y. Wan, S. Tata, O. Seemann, E. Y. Levine, S. Smartsev, E. Kroupp, V. Malka, Femtosecond electron microscopy of relativistic electron bunches. *Light Sci. Appl.* **12**, 116 (2023).
32. C. J. Zhang, J. F. Hua, X. L. Xu, F. Li, C.-H. Pai, Y. Wan, Y. P. Wu, Y. Q. Gu, W. B. Mori, C. Joshi, W. Lu, Capturing relativistic wakefield structures in plasmas using ultrashort high-energy electrons as a probe. *Sci. Rep.* **6**, 29485 (2016).
33. P. E. Masson-Laborde, M. Z. Mo, A. Ali, S. Fourmaux, P. Lassonde, J. C. Kieffer, W. Rozmus, D. Teychenné, R. Fedosejevs, Giga-electronvolt electrons due to a transition from laser wakefield acceleration to plasma wakefield acceleration. *Phys. Plasmas* **21**, 123113 (2014).
34. S. Chou, J. Xu, K. Khrennikov, D. E. Cardenas, J. Wenz, M. Heigoldt, L. Hofmann, L. Veisz, S. Karsch, Collective deceleration of laser-driven electron bunches. *Phys. Rev. Lett.* **117**, 144801 (2016).
35. J. Götzfried, A. Döpp, M. F. Gilljohann, F. M. Foerster, H. Ding, S. Schindler, G. Schilling, A. Buck, L. Veisz, S. Karsch, Physics of high-charge electron beams in laser-plasma wakefields. *Phys. Rev. X* **10**, 041015 (2020).
36. S. Corde, C. Thaury, K. Ta Phuoc, A. Lifschitz, G. Lambert, J. Faure, O. Lundh, E. Benveniste, A. Ben-Ismail, L. Arantchuk, A. Marciniak, A. Stordeur, P. Brijesh, A. Rousse, A. Specka, V. Malka, Mapping the x-ray emission region in a laser-plasma accelerator. *Phys. Rev. Lett.* **107**, 215004 (2011).
37. E. Kroupp, S. Tata, Y. Wan, D. Levy, S. Smartsev, E. Y. Levine, O. Seemann, M. Adelberg, R. Piliposian, T. Queller, E. Segre, K. Ta Phuoc, M. Kozlova, V. Malka, Commissioning and first results from the new 2× 100 TW laser at the WIS. *Matter Radiat. Extremes* **7**, 044401 (2022).
38. W. Lu, M. Tzoufras, C. Joshi, F. S. Tsung, W. B. Mori, J. Vieira, R. A. Fonseca, L. O. Silva, Generating multi-gev electron bunches using single stage laser wakefield acceleration in a 3d nonlinear regime. *Phys. Rev. ST Accel. Beams* **10**, 061301 (2007).
39. C. E. Clayton, J. E. Ralph, F. Albert, R. A. Fonseca, S. H. Glenzer, C. Joshi, W. Lu, K. A. Marsh, S. F. Martins, W. B. Mori, A. Pak, F. S. Tsung, B. B. Pollock, J. S. Ross, L. O. Silva, D. H. Froula, Self-guided laser wakefield acceleration beyond 1 gev using ionization-induced injection. *Phys. Rev. Lett.* **105**, 105003 (2010).
40. A. Pak, K. A. Marsh, S. F. Martins, W. Lu, W. B. Mori, C. Joshi, Injection and trapping of tunnel-ionized electrons into laser-produced wakes. *Phys. Rev. Lett.* **104**, 025003 (2010).
41. C. McGuffey, A. G. R. Thomas, W. Schumaker, T. Matsuoka, V. Chvykov, F. J. Dollar, G. Kalintchenko, V. Yanovsky, A. Maksimchuk, K. Krushelnick, V. Y. Bychenkov, I. V. Glazyrin, A. V. Karpeev, Ionization induced trapping in a laser wakefield accelerator. *Phys. Rev. Lett.* **104**, 025004 (2010).
42. J. M. Dawson, Nonlinear electron oscillations in a cold plasma. *Phys. Rev.* **113**, 383–387 (1959).
43. G.-Z. Sun, E. Ott, Y. C. Lee, P. Guzdar, Self-focusing of short intense pulses in plasmas. *Phys. Fluids* **30**, 526–532 (1987).
44. A. G. R. Thomas, Z. Najmudin, S. P. D. Mangles, C. D. Murphy, A. E. Dangor, C. Kamperidis, K. L. Lancaster, W. B. Mori, P. A. Norreys, W. Rozmus, K. Krushelnick, Effect of laser-focusing conditions on propagation and monoenergetic electron production in laser-wakefield accelerators. *Phys. Rev. Lett.* **98**, 095004 (2007).
45. M. J. V. Streeter, S. Kneip, M. S. Bloom, R. A. Bendoyro, O. Chekhlov, A. E. Dangor, A. Döpp, C. J. Hooker, J. Holloway, J. Jiang, N. C. Lopes, H. Nakamura, P. A. Norreys, C. A. J. Palmer, P. P. Rajeev, J. Schreiber, D. R. Symes, M. Wing, S. P. D. Mangles, Z. Najmudin, Observation of laser power amplification in a self-injecting laser wakefield accelerator. *Phys. Rev. Lett.* **120**, 254801 (2018).
46. C. M. S. Sears, A. Buck, K. Schmid, J. Mikhailova, F. Krausz, L. Veisz, Emittance and divergence of laser wakefield accelerated electrons. *Phys. Rev. ST Accel. Beams* **13**, 092803 (2010).
47. W. Lu, C. Huang, M. M. Zhou, W. B. Mori, T. Katsouleas, Limits of linear plasma wakefield theory for electron or positron beams. *Phys. Plasmas* **12**, 063101 (2005).
48. R. Lehe, M. Kirchen, I. A. Andriyash, B. B. Godfrey, J.-L. Vay, A spectral, quasi-cylindrical and dispersion-free particle-in-cell algorithm. *Comput. Phys. Commun.* **203**, 66–82 (2016).
49. T. Kurz, J. P. Couperus, J. M. Krämer, H. Ding, S. Kuschel, A. Köhler, O. Zarini, D. Hollatz, D. Schinkel, R. D'Arcy, J. P. Schwinkendorf, J. Osterhoff, A. Irman, U. Schramm, S. Karsch, Calibration and cross-laboratory implementation of scintillating screens for electron bunch charge determination. *Rev. Sci. Instrum.* **89**, 093303 (2018).

Acknowledgments: Y.W. would like to thank I. A. Andriyash from Laboratoire d'Optique Appliquée and W. Lu from Tsinghua University for helpful discussions. **Funding:** This work was supported by The Schwartz/Reisman Center for Intense Laser Physics, a research grant from the Benoziyo Endowment Fund for the Advancement of Science, Israel Science Foundation, Minerva, Wolfson Foundation, Schilling Foundation, R. Lapon, Dita & Yehuda Bronicki, and Helmholtz Association. The simulations were carried out at the Weizmann Institute's EXAscale Cluster (WEXAC). **Author contributions:** Y.W. and V.M. conceived the idea and designed the setup. Y.W., O.S., and S.T. together carried out the experiment with support from E.Y.L. and E.K. Y.W. analyzed the data and performed the simulations. Y.W. and V.M. wrote the paper. All authors discussed extensively the results and commented on the manuscript. V.M. provided overall guidance to the project. **Competing interests:** The authors declare that they have no competing interests. **Data and materials availability:** All data needed to evaluate the conclusions in the paper are present in the paper and/or the Supplementary Materials.

Submitted 21 June 2023
Accepted 3 January 2024
Published 2 February 2024
10.1126/sciadv.adj3595